Physics – Uspekhi **62** (7) 633 – 648 (2019)

REVIEWS OF TOPICAL PROBLEMS PACS numbers: **71.27.+a**, **71.30.+h**, **73.20.–r**

Two-dimensional system of strongly interacting electrons in silicon (100) structures

V T Dolgopolov

DOI: https://doi.org/10.3367/UFNe.2018.10.038449

Contents

Abstract. **Studies of various experimental groups that explore the properties of a two-dimensional electron gas in silicon semiconductor systems ((100) Si-MOSFET and (100) SiGe/Si/SiGe quantum wells) in the vicinity of the metal–insulator transition are described and critically analyzed. Results are identified that are common to all research: (i) the effective mass of electrons measured at the Fermi level in the metallic region increases as the electron density decreases and, if extrapolated, tends to diverge; (ii) the behavior of the energy-averaged mass in the metallic region is quite different in the two systems: in Si-MOSFETs, it also exhibits a tendency to diverge, while in the SiGe/Si/SiGe quantum wells it saturates in the limit of low electron densities; (iii) there is a small number (depending on the sample quality) of localized electrons in the metallic phase; (iv) the properties that the electron system exhibits in the insulating phase in the vicinity of the metal–insulator transition are typical of amorphous media with a strong coupling between particles.**

Keywords: two-dimensional electron system, metal–insulator transition, effective mass

V T Dolgopolov
Institute of Solid-State Physics, Russian Academy of Sciences,
ul. Akademika Osipyana 2, 142432 Chernogolovka, Moscow region, Russian Federation;
Editorial Board of *JETP Letters*
E-mail: dolgopolovvalerir@mail.ru, melnikov@issp.ac.ru

Received 28 April 2018, revised 7 October 2018
Uspekhi Fizicheskikh Nauk **189** (7) 673 – 690 (2019)
DOI: https://doi.org/10.3367/UFNr.2018.10.038449
Translated by M N Sapozhnikov; edited by A M Semikhatov

1. Introduction

The review is devoted to a brief description of state-of-the art experimental studies of strongly correlated two-dimensional electron systems based on silicon semiconductor structures. An electron system is called strongly correlated if the characteristic Coulomb interaction energy between electrons greatly exceeds their kinetic (Fermi) energy ε_F. Because the former is inversely proportional to the mean distance between electrons (i.e., $\sqrt{n_s^{-1}}$, where n_s is the electron concentration) and the latter is $\varepsilon_F \propto n_s$, a strong coupling corresponds to low electron concentrations. In most experiments discussed below, the electron gas is assumed to be degenerate, i.e., $\varepsilon_F \gg kT$, where k is the Boltzmann constant and T is the temperature.

The electron–electron interaction strength is usually characterized by a parameter r_s equal to the ratio of the Wigner–Seitz radius $(\pi n_s)^{-1/2}$ to the Bohr radius of the electron $a_B = \kappa\hbar^2/(me^2)$, where κ is the dielectric constant determining the interaction between electrons, and m and e are their mass and charge. In the simplest case of a single-valley electron system (which does not include the electron systems considered below), r_s is equal to the ratio of the characteristic potential interaction energy to the Fermi energy.

For the readers who are not familiar with the properties of silicon-based two-dimensional electron structures, we present some required information very schematically. In the momentum space, the Wigner–Seitz cell for silicon is a truncated octahedron (Fig. 1a). The center of the Wigner–Seitz cell is denoted by Γ, the center of squares by X, and the center of hexagons by L. The minima of the conduction band are located on straight lines connecting points Γ and X. There are six such points altogether. The isoenergy surfaces in the momentum space are shown schematically in Fig. 1b. They are ellipsoids of revolution with a mass of $0.98m_0$ along the major axis (m_0 is the free electron mass)

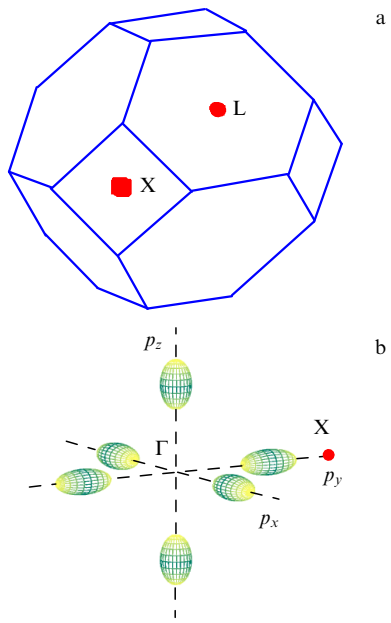

Figure 1. (a) Wigner–Seitz cell for electrons in silicon. (b) Image of constant-energy surfaces near the minima of the conduction band.

and $m_b = 0.19m_0$ for the momentum in the perpendicular direction.

If potential barriers are introduced making the electron motion in the z-direction restricted (for the (100) sample orientation), discrete levels appear in such a quantum well, the lowest of them being determined by ellipsoids with the major axis directed along z (with the 'heavy' mass corresponding to the motion along z). There are two such ellipsoids, and therefore the spectrum of the form

$$\varepsilon(p) = \varepsilon_0 + \frac{p^2}{2m_b}\,, \tag{1}$$

where ε_0 is the energy of the lowest level in the quantum well and p is the momentum in the (100) plane, has the so-called 'valley' degeneracy in addition to spin degeneracy. Strictly speaking, the valley degeneracy is lifted in an asymmetric potential well; however, we ignore this small splitting in what follows.

To fill a potential well with electrons, the Fermi energy ε_F must exceed ε_0. With this condition fulfilled, electrons freely moving along the quantum well appear with the wave function spreading in the z direction by 30 Å in Si-MOSFETs and by 150 Å in SiGe/Si/SiGe quantum wells considered in Section 3.

The two electron systems considered here have another substantial difference. In silicon MOSFETs, electrons are localized at the interface between silicon, with the dielectric constant κ_{Si}, and silicon dioxide (κ_{SiO_2}). Therefore, the interaction between electrons is determined by the mean dielectric constant $(\kappa_{Si} + \kappa_{SiO_2})/2 \simeq 7.7$. In the SiGe/Si/SiGe quantum well, the interaction is determined by the dielectric constant κ_{SiGe} close to κ_{Si}. Therefore, to achieve the same interaction in SiGe/Si/SiGe, it is necessary to reduce the electron concentration by at least a factor of 2.5.

The current carrier concentration is controlled with a metal electrode (gate) deposited on the dielectric separating a two-dimensional electron layer from the gate. The electron concentration depends linearly on the potential difference between the gate and the electron layer. We show below that the gate allows obtaining information on many properties of the electron system.

2. Electrons in (100) Si-MOSFET transistors

2.1 Metal–insulator transition in the absence of a magnetic field

Two-dimensional electron systems at liquid helium temperatures can have a high conductivity considerably (by more than two orders of magnitude) exceeding $\sigma_0 = e^2/h$ (where e is the electron charge and h is Planck's constant). However, at low electron densities, real electron systems exhibit a low conductivity $\sigma \ll \sigma_0$, with the activation temperature dependence typical of an insulator.

Beginning with paper [1] based on the scaling hypothesis, it has become commonly accepted that a metal phase in a two-dimensional electron system (even with an arbitrarily weak disorder) is impossible in the sense that such a system with infinite dimensions at zero temperature would inevitably become an insulator. In this case, the metal–insulator transition (MIT) in a two-dimensional system turned out to be impossible, and the experimentally observed transition was called 'apparent'. The term is slightly misleading because 'apparent' should rather refer to an insulator assumed in the place of a metal at unrealistically low temperatures and fantastically huge dimensions of the sample.

A revolutionary role was played by experiments [2, 4] in which the unusual temperature behavior of the resistance of highly mobile electrons in Si-MOSFET was observed in the vicinity of the transition from the metal dependence to the behavior typical of an insulator (Fig. 2). In fact, such a behavior was observed even earlier in [3], remaining unnoticed, however.

It was found in [2, 4] that curves in the metal region, as well as in the insulator region, can be scaled into one universal curve. These two groups of curves are separated by a temperature-independent line corresponding to the concentration $n_c = 7.25 \times 10^{10}$ cm^{-2} in Fig. 2. By extrapolating this line to the zero temperature, we see that the MIT in the electron system under study is possible, even at a zero temperature, in samples with infinite dimensions, which obviously contradicts paper [1]. Because at electron concentrations of the order of 10^{11} cm^{-2} the kinetic (Fermi) energy in

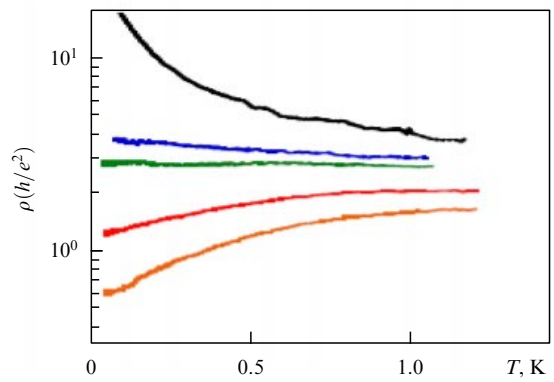

Figure 2. Temperature dependences of Si-MOSFET sample resistance at electron densities (from top to bottom) of 6.85, 7.17, 7.25, 7.57 ($\times 10^{10}$) cm^{-2} (from data in [5]).

the electron gas under study is an order of magnitude lower than the characteristic electron–electron interaction energy, this contradiction was interpreted to be the result of a strong coupling between electrons. It seemed that a one-parameter scaling remained valid with a scaling function changed by the interaction. The conviction that a one-parameter scaling remains universal has led to paradoxical conclusions [6, 7] that a two-dimensional electron system remains metallic even for resistances of the order of $3 \times 10^7\ \Omega$ per square and a positive temperature derivative of the conductivity and that the critical concentration n_c can decrease with increasing disorder.

At the same time, more realistic renormalization group calculations have appeared taking renormalization with the increasing coupling strength and disorder into account [8–12]. Based on such calculations, a conclusion was made that the phase transition observed in the most perfect Si-MOSFET is indeed a quantum phase transition [10, 11]. Experimental data were consistent with the theory in the metal region [12–14]. Paper [14] is of interest because it describes the experimental temperature dependence in a considerably broader range than the theory of small corrections does [15, 16].

The subject of MITs, in particular, transitions in highly mobile MOSFETs, has been considered in many reviews [6, 17–23, 25]. We do not review their content but only note some details.

(i) We first note that the critical concentration n_c is not universal and changes upon changing the random potential (see Figs 2 and 3a and also [25]).

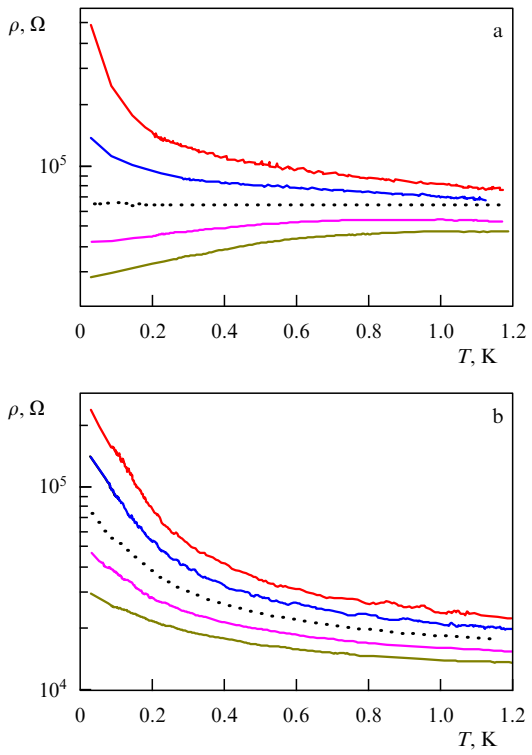

Figure 3. Temperature dependences of the resistance of an Si-MOSFET sample in the absence of a magnetic field (a) at electron densities (from top down) 7.65, 7.80, 7.95, 8.10, 8.25 ($\times 10^{10}$) cm^{-2} and in the 4 T magnetic field parallel to the interface and (b) at electron densities 1.095, 1.125, 1.155, 1.185, 1.215 ($\times 10^{11}$) cm^{-2} (from data in [24]).

(ii) If we assume that the transition discovered in Si-MOSFET is a quantum MIT stabilized due to interaction, then there must be another MIT appearing as the electron concentration increases and the interaction weakens. But no trace of such behavior was observed (see, e.g., [26]). However, the possible absence of the second transition was theoretically predicted in [10].

(iii) Despite a certain success, the renormalization group theory cannot offer any predictions about the structure of an insulator.

2.2 Influence of a magnetic field on the metal–insulator transition

A magnetic field parallel to the interface acts only on the spin of electrons in a two-dimensional electron system and can completely spin-polarize it [27]. The spin-polarized electron system in the vicinity of the transition changes its behavior from that typical of a metal to that typical of an insulator and does not exhibit any properties similar to those shown in Fig. 2. We can see from Fig. 3b that the resistance increases with decreasing temperature at all electron concentrations, although a number of features (the disappearance of nonlinearity, the vanishing of the activation energy) demonstrate the transition from an insulator to a metal at the critical concentration $n_c = 1.155 \times 10^{11}$ cm^{-2}. Strictly speaking, a nonhorizontal separatrix separating the metal from insulator does not mean the absence of a quantum phase transition (this question is discussed in detail in [6, 23]). Therefore, the determination of the critical concentration by the sign of the temperature derivative is at least controversial. Below, we use other criteria for finding the critical concentration n_c, for example, by the vanishing of the activation energy in the insulator phase.

Figure 4 shows the position of the MIT point in the (B, n_s) plane in a magnetic field normal and parallel to a two-dimensional electron gas. In the parallel orientation of the magnetic field, the transition point position is independent of the angle between the current and field, which again confirms the influence of the magnetic field, in this case only on the spin of electrons. (The contribution of orbital effects to the magnetoresistance in Si-MOSFET is rather weak: in [28], a magnetoresistance anisotropy of about 5% was observed in the parallel field for different current directions with the respect to the field.)

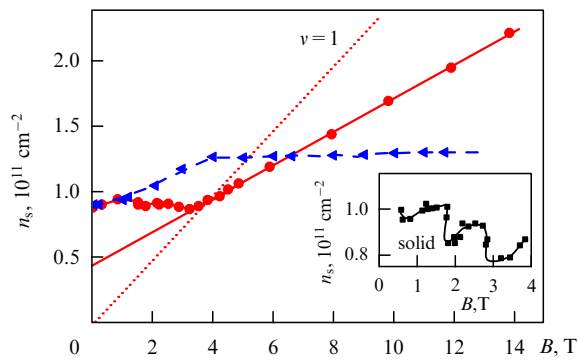

Figure 4. Critical density for the MIT measured for two orientations of a magnetic field: perpendicular to the interface (from data in [29]) (dots) and parallel to the interface (triangles). $n_c(B = 0) = 0.89 \times 10^{11}$ cm^{-2}. The dashed straight line corresponds to the filling factor $\nu = 1$. The inset shows critical density oscillations on an expanded scale [30].

In the region under the solid line in Fig. 4 in the normal magnetic field and under the dashed line in the parallel field, the electron system is an insulator, while above these lines it is a metal. Two points must be noted. First, the critical concentration in the parallel magnetic field gradually increases by approximately a factor of 1.5 and then ceases to increase with increasing the magnetic field. Second, the behavior of the critical density proves to be quite different in the normal and parallel magnetic fields.

The increase in the critical concentration in the parallel magnetic field is related to the spin polarization of electrons. In a strong magnetic field (exceeding 4 T in Fig. 4), electrons are completely spin-polarized and the critical density is independent of the magnetic field. The transition from a spin-polarized electron insulator to a spin-polarized metal was observed in [31].

The last statement, as well as the scale of the effect and the resistance behavior in the metal region agree with the concept of the MIT due to multiple electron–electron scattering [32]. In the metal phase, a high-viscosity region appears, which was called a metal glass in [33]. A similar region, although in a considerably narrower concentration range, can also exist in a zero magnetic field. In any case, it is distinctly observed in strongly disordered Si-MOSFETs [6].

The linear increase in the critical concentration in the initial region in Fig. 4 in the framework of these concepts should correspond to the behavior of the field corresponding to complete spin polarization, which, even if not quite exactly, corresponds to experiments. Nevertheless, the correctness of the description of the MIT in most perfect Si-MOSFETs based on calculations in [32] is doubtful. These calculations correspond to the Anderson transition rather than to a quantum transition. In addition, the transition point in calculations is determined by extrapolation from the metal region.

The linear dependence of the critical concentration in a strong normal magnetic field can be understood based on considerations presented in [34]. The normal magnetic field reduces the amplitude of zero vibrations of electrons in an insulator ($\propto B^{-1/2}$). According to the Lindeman criterion, the critical electron density is determined by comparing the amplitude of zero vibrations and the interelectrode distance ($\propto n_s^{-1/2}$). The extrapolation of the straight line to the zero magnetic field specifies the number of localization centers equal to 4×10^{10} cm^{-2} for Fig. 4.

In the initial region, where quantization is insignificant, curves for normal and parallel magnetic fields coincide. But as the magnetic field is increased further, the critical electron density of the MIT in the normal field does not increase, in contrast to the case of a parallel field, and even somewhat decreases, exhibiting small oscillations (see the inset in Fig. 4).

In a strong quantizing magnetic field, each of the quantum levels has a band of delocalized states. As the magnetic field decreases, the delocalized states lower in concentration, each of them following its filling factor. Therefore, the MIT in a strong field should occur when the filling factor is smaller than unity (see Fig. 4). In a weak magnetic field ($\omega_c\tau \simeq 1$), delocalized states detach from quantum levels and, being topologically protected, merge, not decreasing their energy or concentration with a further decrease in the field [35, 36].

The boundary oscillations in this region were explained by the chemical potential oscillations under conditions of the quantum Hall effect [37, 38]. It was assumed that both phases can coexist at the MIT boundary. In this case, the chemical potentials of the phases must be equal at the transition point. The chemical potential of the insulator changes gradually with energy, whereas the chemical potential of the metal in a quantizing magnetic field oscillates, resulting in boundary oscillations.

2.3 Electron properties in the depth of the Fermi distribution

2.3.1 Complete spin polarization field. *Experiment*. The complete spin polarization field B^p parallel to a surface depends linearly on the electron density [39–41] and vanishes when extrapolated to zero at the finite electron concentration n_{c0} (Fig. 5). The linear dependence, which was first established from transport measurements, was later confirmed in independent experiments [42]. It was shown in [41] that sample quality worsening did not change the slope of the linear dependence but increased n_{c0}. Because n_{c0} proved to be rather close to n_c in all experiments, it was assumed that the number of mobile electrons was not n_s but only $n_s - n_c$.

To rule out such a possibility, the electron density n_{Hall} was measured in [39] by the Hall effect in a weak magnetic field (Fig. 6). The electron concentration measured in these experiments turned out to be coincident within the experimental accuracy with the total electron concentration n_s determined, as usual, by the Shubnikov–de Haas effect in a

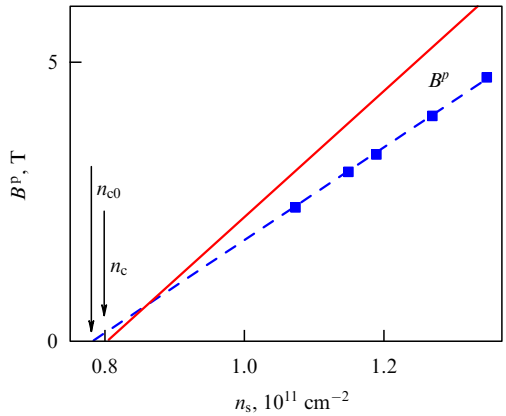

Figure 5. Dots: total spin-polarization field as a function of the electron concentration (from data in [39]). The dashed line is a least-square fit of experimental points. The solid line is the expected result for noninteracting electrons in the model presented in the text.

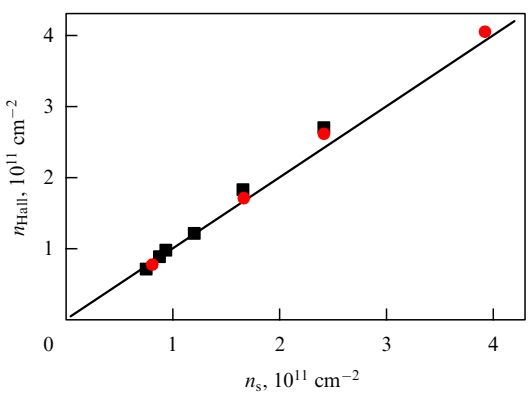

Figure 6. Electron concentration from Hall effect measurements in a weak magnetic field as a function of the total electron concentration determined by quantum oscillations in a strong magnetic field. Dots $B = 0.3$ T, squares: $B = 0.1$ T. The solid line corresponds to $n_{Hall} = n_s$.

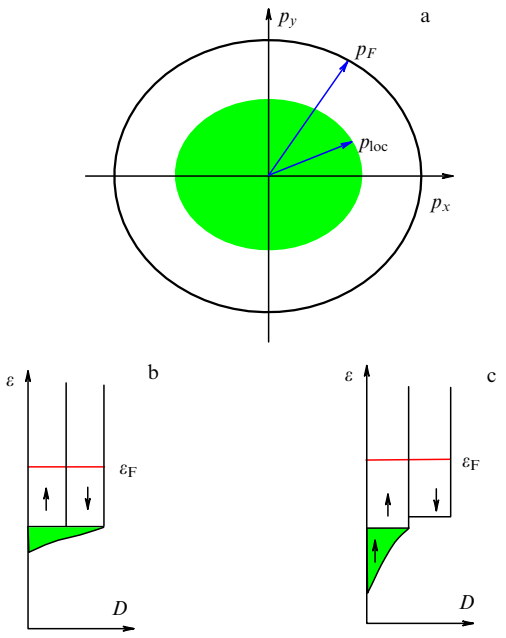

Figure 7. (Color online.) (a) Fermi surface with localized states inside (green filling). (b) Density of states $D(\varepsilon) = \mathrm{d}n/\mathrm{d}\varepsilon$ as a function of energy. Localized states (green filling) in the absence of a magnetic field are not spin-polarized. (c) Density of states as a function of energy in a weak magnetic field. Localized states are completely spin polarized.

strong magnetic field. Below, we will show that such an experiment does not necessarily rule out the existence of a 'tail' of the density of states containing localized electrons.

The condition of the total spin polarization can be formulated as follows: the Fermi energy referenced to the bottom of the electron subband for electrons gaining the energy ε_F^p in the magnetic field is $\mu_B g B^p$ (here, μ_B is the Bohr magneton and g is the Lande factor taken at the energy ε_F^p). The constant slope of the experimental dependence in Fig. 5 means that $\mu_B g D_T^p = \text{const}$. Here, the Lande g-factor and the thermodynamic density of states (D_T^p) of the totally spin-polarized electron gas are, in principle, functions of the electron density. Taking into account that the g-factor weakly changes with the electron density in the metal phase, the constant slope means the absence of the renormalization of the thermodynamic density of states in the totally spin-polarized electron system of (100)Si-MOSFET.

The discovery of a finite critical density even in the most perfect silicon structures was interpreted as a manifestation of the possible spontaneous spin polarization in a strongly interacting electron gas or at least as magnetic-field-induced instability [22, 39].

The naïve model. The behavior of the total spin polarization field, similar to that shown by dots in Fig. 5, can also be realized in a two-dimensional system of noninteracting electrons. Indeed, we assume that some of these electrons are localized (Fig. 7). In a zero magnetic field, two spin subbands are filled equally, each of them consisting of two valley subbands. The tail of spin-localized states is not polarized.

It is important that (i) the first delocalized electron has a finite quasimomentum and energy (Fig. 7a):

$$p_{loc} = \hbar(\pi n_c)^{1/2}, \qquad \varepsilon(n_c) = \frac{p_{loc}^2}{2m^*}, \tag{2}$$

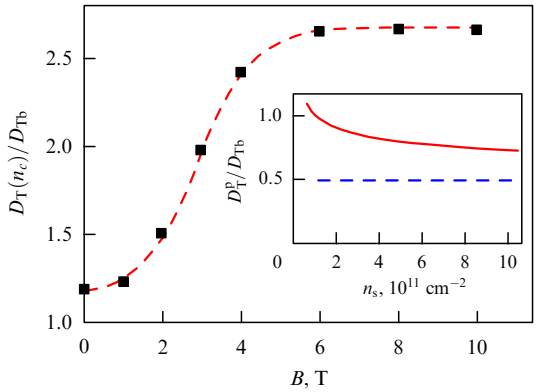

Figure 8. Thermodynamic density of states in the vicinity of the critical concentration in the insulator phase in a parallel magnetic field (from data in [24]). The inset is the thermodynamic density of states for completely spin-polarized electrons in the metal phase for experimental data in Fig. 5 (dashed curve) and results on [49] (solid curve).

and (ii) the number of strongly localized electrons is independent of n_s ($n_s > n_c$).

Equation (2) cannot be proved, is an assumption, and should be verified experimentally. The question about the possibility of verifying this equation is considered in the next sections.

In a weak magnetic field and at a sufficiently low temperature, all electrons in the 'tail' are spin polarized (Fig. 7c). This is possible, for example, for single localized spins [43, 44]. The analog of Fig. 7a cannot be drawn for Fig. 7c.

The attempt to measure the thermodynamic density of states in a spin-polarized localized electron system [24] has led to an entirely unexpected result, shown in Fig. 8. The thermodynamic density of states of a spin-polarized electron system in the insulator phase turned out to be almost three times higher than that for spin-nonpolarized electrons and almost six times greater than for spin-polarized electrons.

The polarization of mobile electrons begins at concentrations $n_s > n_c$. In other words, in the model considered here, $n_c = n_{c0}$, and the slope of the straight line is determined by the condition

$$\frac{\mathrm{d}B^p}{\mathrm{d}n_s} = \frac{2}{\mu_B g D_{Tb}} = \frac{\pi\hbar^2}{m^*\mu_B g}, \tag{3}$$

where $D_{Tb} = 2D_{Tb}^p = \mathrm{d}n_s/\mathrm{d}\varepsilon_F$ is the thermodynamic density of states of the spin-nonpolarized electron gas with band parameters. The corresponding dependence is shown by the solid straight line in Fig. 5 for $m^* = m_b$ (m_b is the band electron mass), $g = 2$. We can see from Fig. 5 that the values of n_c and n_{c0} virtually coincide and the slope of the experimental straight line is smaller than expected. The slopes can be matched assuming that the g-factor exceeds the band g-factor: $g = 1.3g_0 = 1.3 \times 2$. Indeed, the measured values of the Lande g-factor always exceed g_0, being $(1.5-1.7)g_0$ [45], $1.5g_0$ [47], and $(1-1.3)g_0$ [48]. All these values were obtained from measurements in a normal magnetic field and therefore it is not obvious that the same values of the Lande g-factor are also applicable to the magnetic field parallel to the interface.

We note that the presence of localized states satisfying Eqn (2) cannot be found in transport measurements in the

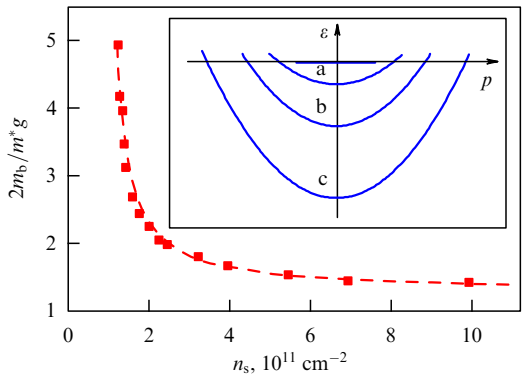

Figure 9. Electron concentration dependence of the average single-particle mass m^* multiplied by the Lande g-factor at the Fermi level for spin-polarized electrons (from data in [39]). The inset shows single-particle electron spectra for three electron concentrations (c) n_s, (b) $2n_s$, (a) $4n_s$. Energies are determined from the Fermi level.

metal phase, where all the properties are determined by the close vicinity of the Fermi surface. In particular, measurements of the Hall resistance in weak magnetic fields give the total electron concentration.

The assumption that the electron system undergoes a transition to the totally spin-polarized state is also well founded because, for example, a system of localized magnetic moments is already polarized at zero temperature in an infinitely weak magnetic field.

These considerations can be applied with minor changes to a system of strongly interacting electrons, assuming that we are dealing with single-particle electron states. The average mass of quasiparticles in this model is independent of (or weakly depends on) the electron concentration. Such a model was probably used to interpret experimental results in [41, 46].

The alternative naïve model consists of the following. It is assumed that when the critical concentration n_c is exceeded, all electrons become mobile and the energy of a totally polarized gas vanishes at n_c:

$$p(n_s) = \hbar(\pi n_s)^{1/2}\,, \quad \varepsilon_F^p(n_s) = \frac{p^2}{2m^*} \propto (n_s - n_c)\,. \tag{4}$$

The assumed single-particle spectrum of a completely polarized electron gas is shown schematically in the inset in Fig. 9. The spectrum is quadratic, with the average effective mass m^*. The constant value of the thermodynamic density of states and the vanishing of the total spin polarization field at $n_s = n_c$ cause the divergence of m^*, as shown in Fig. 9.

This model was earlier used in a number of papers beginning with [39] and ending with recent study [22].

Both models have a number of disadvantages. First, quasiparticles are treated as free particles even in the depth of the Fermi distribution. Neither model can explain the shift of the critical concentration as the total spin polarization sets in. Finally, they do not consider the physical properties of an insulator.

2.3.2 Thermodynamic density of states. As mentioned above, the thermodynamic density of states is one of the parameters that can be inferred from experiments. Experimental data for a completely polarized system of mobile electrons can be compared with the results of numerical Monte Carlo simulations [49]. The solid curve in Fig. 8 shows the thermodynamic density of states of an ideal two-dimensional Si-MOSFET electron system with the electron scattering ignored, calculated using the results in [49]. The dashed line in the inset shows the thermodynamic density of states obtained from experimental data in Fig. 5 using the value $g = 1.3g_0$. We can see from Fig. 8 that the calculated thermodynamic density of states weakly depends on the electron density for $n_s > 3 \times 10^{11}$ cm^{-2}, asymptotically approaching the dashed line as $n_s \to \infty$. The complete spin polarization field calculated in the same concentration region is consistent with experiment. According to [49], the consideration of a finite mean free path of electrons reduces the growth of the thermodynamic density of states at minimal electron concentrations, such that the thermodynamic density of states approaches a constant in the concentration range of interest to us.

A comparison of the data in Fig. 8 with that in the inset shows that the thermodynamic density of states in the parallel magnetic field experiences a jump at the concentration n_c, increasing under conditions of the complete spin polarization in the insulator phase.

Information on the thermodynamic density of states can be obtained from the MOSFET capacitance measurements. Indeed, by measuring capacitances in the absence of a magnetic field and in a field parallel to the plane of a two-dimensional system, we determine their difference $\Delta C(n_s)$ in the region of complete spin polarization,

$$\frac{\Delta C}{C} = C_0(Ae^2)^{-1}\left(\frac{1}{D_{\mathrm{Tpol}}} - \frac{1}{D_{\mathrm{T}}}\right), \tag{5}$$

where A is the gate area. For an electron density lower than 1.2×10^{11} cm^{-2}, the electron system in a magnetic field becomes an insulator, resulting in an increase in $|\Delta C|$. At the electron concentration 2.25×10^{11} cm^{-2}, the transition to the completely spin-polarized state from magnetoresistance measurements is detected.

We can see from Fig. 10 that the measured capacitance difference decreases as the electron concentration increases. This is possible only if the thermodynamic density of states

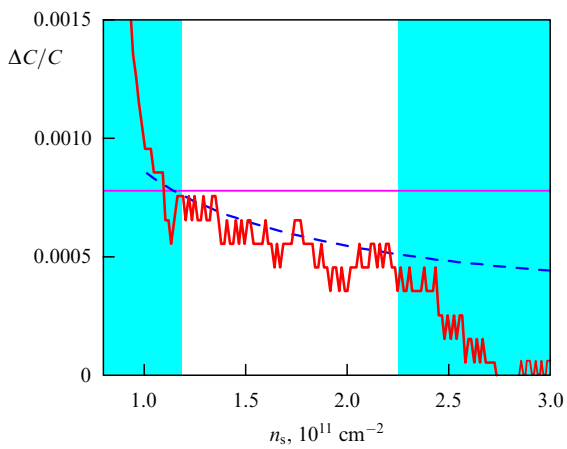

Figure 10. MOSFET-capacitance-normalized difference of capacitances measured in the absence of a magnetic field and in the 9.9 T parallel magnetic field. The solid straight line shows the level expected for the electron system without interaction. Experimental data should be considered only in the unfilled region. The dashed curve is a fit of the capacitance with Eqn (5) taking the possible change in the thermodynamic density of states $D_{\mathrm{T}} \propto n_s/(n_s - n_c)$ into account [5]. The last expression should be regarded as a purely empirical one, properly describing experimental data.

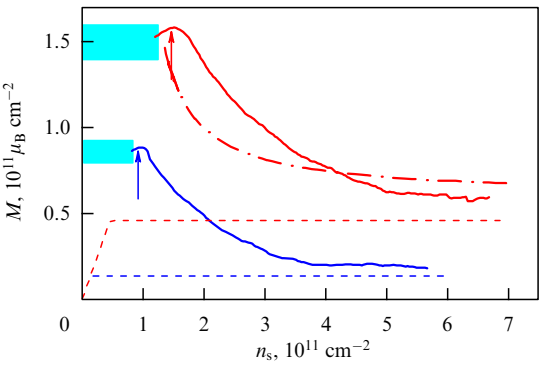

Figure 11. Electron concentration dependences of the magnetic moment of the unit area in the 5 T (top solid curve) and 1.5 T (bottom solid curve) parallel magnetic fields, $T = 0.4$ K (from data in [42]). The dashed line shows the expected behavior of the magnetic moment in the same fields for a free-electron gas with band parameters. The arrows show concentrations corresponding to the total spin polarization (from data in Fig. 5). The dashed-dotted curve is calculated in the parabolic dispersion approximation with the same average effective mass of electrons with different spin orientations. The Lande g-factor and mass correspond to Fig. 9. Insulator regions are colored.

behaves as $D_T \propto n_s/(n_s - n_c)$ and $D_{Tpol} = \text{const}$.[1] Such a behavior was reported in [51] based on the analysis of data on the dependence of the elastic relaxation time on the electron density. The fitting of experimental data with this expression and Eqn (5) is shown by the dashed line in Fig. 10 for $D_T = D_{Tb} n_s/(n_s - n_c)$ and $D_{Tpol} = D_{Tb}/1.3$. The result obtained should be verified by measurements in stronger magnetic fields.

2.3.3 Electron magnetic moment in the metal phase. Studies of the electron magnetic moment were initiated in [52]. Because the direct measurement of the magnetic moment of a two-dimensional electron system is difficult due to its smallness, the quantity $\partial\mu/\partial B$, equal to $-\partial M/\partial n_s$ according to Maxwell's relation, was measured in experiments. Here, μ is the chemical potential of the electron system and M is the magnetic moment of the unit area. To obtain the dependence $M(n_s)$, the measured quantity should be integrated over the electron concentration. However, to do this, it is necessary to use some point with the known magnetic moment as the initial point or to measure $\partial\mu/\partial B$ in the insulator region at low electron densities for the most perfect samples, which is not simple at low temperatures. Below, we present results obtained by the first [42] and second [52–55] methods.

The magnetic moment as a function of the electron density for two magnetic fields is shown in Fig. 11. The curves shown in this figure were obtained from original curves by integrating, assuming that interaction can be disregarded at the maximal electron concentration and the band mass and the Lande factor $g = 1.3g_0$ can be used for calculating the magnetic moment. This procedure is justified by the fact that near the maximum, the magnetic moment expressed in Bohr magnetons coincides with good accuracy with the total number of electrons (the discrepancy does not exceed 2×10^{10} cm^{-2}).

[1] The expression for D_{Tpol} obtained in [50] is based on a misunderstanding: chemical potentials entering Maxwell's relation and screening were measured relative to different levels.

For comparison, the dashed lines in Fig. 11 show the dependences of the magnetic moment expected for a gas of free electrons with band parameters. We can see that interaction plays a considerable role and significantly modifies the dependence $M(n_s)$. In addition, the dashed-dotted curve in Fig. 11 shows the expected dependence for a gas of interacting electrons, assuming that electrons with oppositely oriented spins have a parabolic spectrum with a mass $\propto n_s/(n_s - n_c)$. We can see that the spectrum of a partially polarized electron system is not quadratic, and a comparison of the values of two solid curves at an arbitrary fixed concentration suggests that the degree of spin polarization is approximately proportional to the magnetic field.

Recently, a method for measuring the magnetic moment in an insulator was proposed in [55]. Measurements are possible at a low but finite conductivity at a finite temperature. The method is based on the fact that MOSFET charging occurs in the same way under modulation of the gate voltage and parallel magnetic field. In the first case, some effective capacitance is measured (which depends on the conductivity and does not exceed the sample capacitance), and in the second case the value of $\partial\mu/\partial B$ related to the same area as that the measured capacitance is determined. The only unwelcome feature of the method is that the magnetic moment measured is related to the near-contact region of the sample.

One of the results in [54], obtained by integrating the magnetic moment starting from the zero electron density, at which the magnetic moment of the electron system is zero, is shown in Fig. 12. The curve presented in the figure is consistent in the overlap region ($n_s < 6 \times 10^{11}$ cm^{-2}) with data obtained earlier by a different method [52] for which the magnetic moment is approximately proportional to the magnetic field and is therefore mainly caused by mobile electrons. As the electron density is increased further, the magnetic moment ceases to decrease (Fig. 12). The level at which the dependence $M(n_s)$ is saturated depends weakly on the temperature and the magnetic field strength (see the inset in Fig. 12), which is without a doubt related to the presence of localized electrons in the metal phase and which allows estimating their number. Indeed, because the magnetic moment at saturation depends on the temperature very

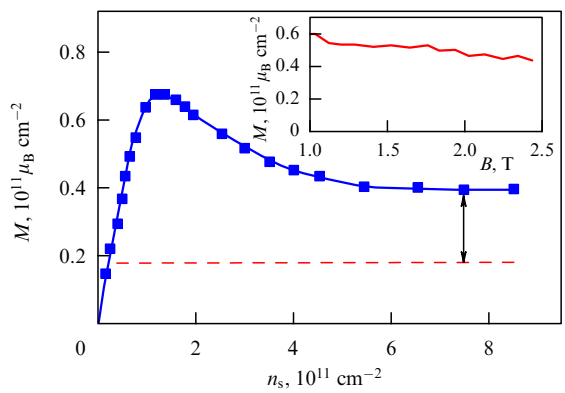

Figure 12. Concentration dependence of the magnetic moment of the unit area in the 2 T parallel magnetic field at the temperature 1.7 K (squares). The dashed straight line shows the expected behavior of the magnetic moment in the same fields for a free-electron gas with band parameters. The arrow corresponds to the maximum number of localized electrons in the metal phase. The inset demonstrates the dependence of the magnetic moment on the magnetic field at the electron concentration 4.3×10^{11} cm^{-2} (from data in [54]).

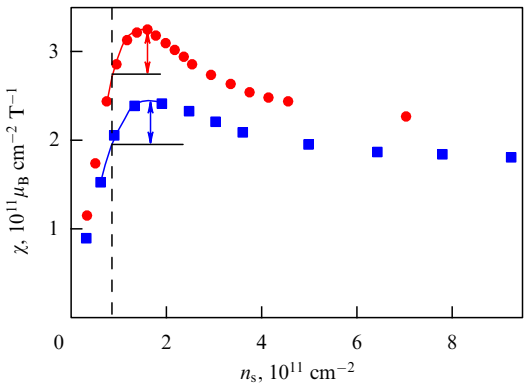

Figure 13. Dependences of the magnetic susceptibility in the zero magnetic field on the electron density for two samples from different manufacturers (dots: samples made in Russia, squares: a sample from Holland). The vertical dashed straight line indicates the MIT, $T = 1.7$ K (from data in [54]).

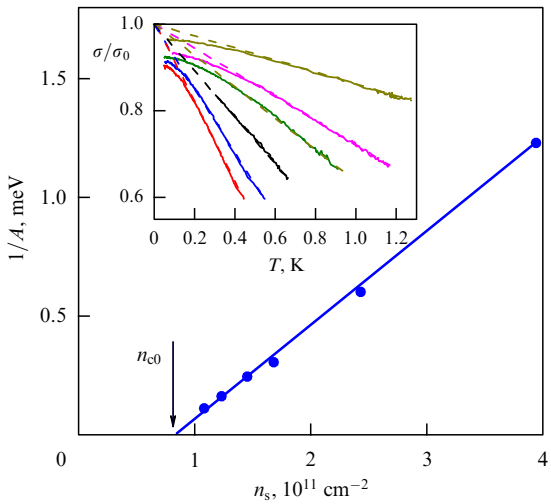

Figure 14. Inverse slope $1/A$ of the temperature dependence of the normalized conductivity as a function of the electron density. The inset shows the temperature dependence of the normalized conductivity at the electron concentrations (from top down) 2.4, 1.68, 1.45, 1.23, 1.08, and 1.01 ($\times 10^{11}$ cm^{-2}) (from data in [47]).

weakly, the maximum number of localized electrons is equal to the difference between the saturation level and the expected level for a free electron gas. It is 2×10^{10} cm^{-2}, whereas $n_c = 8.5 \times 10^{10}$ cm^{-2} for the sample under study. This number is not universal. It changes from sample to sample and can change from cooling to cooling, even for one sample.

Many efforts have been made to study the magnetic susceptibility, i.e., the quantity $\chi = \partial M/\partial B$ $(B = 0)$ (Fig. 13). A comparison of the result presented in Fig. 13 with a rough estimate of the expected magnetic susceptibility according to the data in Figs 11 and 12 shows that the measured susceptibility exceeds the expected one by almost an order of magnitude. This is possible only if the magnetic susceptibility is caused by the initial stage of the rearrangement of the 'tail' of the density of states (see Fig. 7) and is not directly related to the properties of delocalized electrons.

We note two features of the curves in Fig. 13. First, the curve obtained for a sample from the Netherlands lies below the corresponding curve for a sample made in Russia. Assuming that with all other parameters equal, the susceptibility in the metal phase is proportional to the number of localized electrons, we can conclude that the number of localized electrons in the Russian sample is greater by 25%.

Second, the susceptibility in a small concentration interval continues to increase with increasing n_s in the metal phase, and this increase is virtually the same for both samples (arrows in Fig. 13).

2.4 Electron properties at the Fermi level

2.4.1 Temperature dependence of the conductivity. In the absence of a magnetic field, the conductivity of a two-dimensional electron system linearly depends on temperature in some temperature range. Such a behavior of the conductivity was predicted by two different models [15, 16, 56] and experimentally demonstrated in [57]. The temperature interval in which a linear dependence is expected is determined by the condition

$$\frac{\hbar}{\tau} \ll kT \ll p_F v_F\,, \tag{6}$$

where k is the Boltzmann constant, and p_F and v_F are the electron momentum and velocity on the Fermi surface. The left inequality in relation (6) corresponds to the ballistic regime [16]. It appears in the alternative model [15] as the restriction on energy in the regime where the screening parameter is washed out by collisions.

It is important for us that independently of the model, the conductivity in the linear region is determined by the relation

$$\frac{\sigma(T)}{\sigma(0)} = 1 - AkT\,, \tag{7}$$

where $A \propto (p_F v_F)^{-1} \propto m_F^*/n_s$. Here, we standardly introduce the single-particle mass on the Fermi surface as $m_F^* = p_F/v_F$.

Examples of the temperature dependence of the conductivity on the metal side of the MIT are shown in the inset in Fig. 14. For each of the electron concentrations, the temperature dependence of the conductivity has a linear region that allows determining $A(n_s)$. This dependence is shown in Fig. 14. The dependence $1/A(n_s)$ is linear with good accuracy and can be extrapolated to a finite concentration coinciding for the sample under study with n_{c0} and n_c. The linear dependence means that $m_F^* \propto n_s/(n_s - n_c)$, similarly to the behavior of the mean mass of spin-polarized electrons, and by extrapolation diverges at the same concentration where the Fermi energy of spin-polarized electrons reaches the bottom of the electron subband (see Fig. 5).

2.4.2 Thermal EMF. The alternative method for studying the electron properties in the vicinity of the Fermi level in Si-MOSFET involved measurements of the thermal EMF $S_T = -\Delta V/\Delta T$ [58], where ΔV is the potential difference caused by the temperature difference ΔT for a constant thermal flow directed along the electron layer. The creation of such a thermal flow and control of its constancy are the major experimental challenges in measuring the thermal EMF at low temperatures.

In the case of noninteracting electrons (taking valley degeneracy into account), the thermal EMF is described by the expression

$$S_T = -\frac{2\pi k^2 m_b T}{3e\hbar^2 n_s}\,. \tag{8}$$

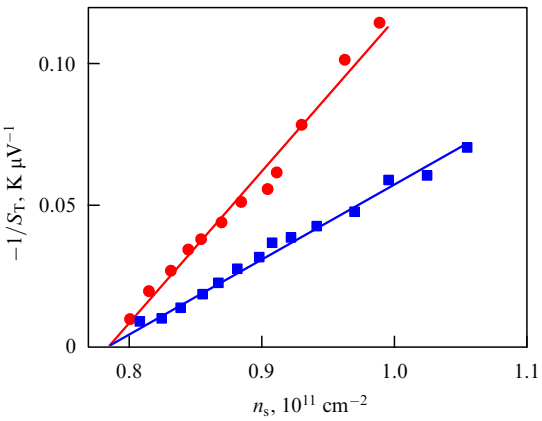

Figure 15. Dependences of the inverse EMF on the electron concentration at 300 mK (dots) and 600 mK (squares). The straight lines drawn through the points are extrapolated to the concentration n_{c0} (data from [47]).

At a low electron density, the elastic relaxation time itself becomes temperature dependent [15, 16], resulting in a correction to Eqn (8). In the right-hand side, an additional factor appears depending on the disorder [59–61] and interaction [62]. In addition, for interacting electrons, m_b should be replaced with m_F^* in Eqn (8). It is expected that $1/S_T$ is inversely proportional to the temperature and in the simplest case proportional to n_s/m_F^*.

Indeed, experiments demonstrate the correct scaling of the thermal EMF with the temperature and a linear dependence of the inverse EMF on the electron density (Fig. 15).This implies a constant value of the additional factor in Eqn (8) caused most likely by the narrowness of the electron concentration interval in which the measurements were performed.

The thermal EMF measurements confirm the dependence $m_F^* \propto n_s/(n_s - n_c)$ at minimal achievable electron densities and extend it much closer to the critical concentration.

2.4.3 Entropy measurements. Additional information on the properties of the electron system in Si-MOSFET was obtained from entropy measurements [63]. Rather complicated experiments involved the study of the response of the chemical potential of the electron system to the temperature modulation $\Delta\mu/\Delta T$ equal to the change in entropy with the opposite sign after the addition of one electron. The entropy S of the unit area of a degenerate noninteracting electron gas ($kT \ll \varepsilon_F$, where ε_F is the Fermi energy measured from the bottom of the electron subband) is

$$S = \frac{k^2 \pi T g_s g_v m_b}{6\hbar^2} \tag{9}$$

and is independent of the number of electrons. Therefore, the zero response is expected for noninteracting electrons.

The properties of a degenerate electron gas of interacting electrons are determined by the nearest vicinity of the Fermi level [64]:

$$\frac{\partial S}{\partial n_s} = \frac{\partial m_F^*}{\partial n_s} \frac{k^2 \pi T g_s g_v}{6\hbar^2} . \tag{10}$$

Because the electron mass at the Fermi level increases with decreasing the electron density, the negative values of $\partial S/\partial n_s$ are expected in the region of the degenerate gas.

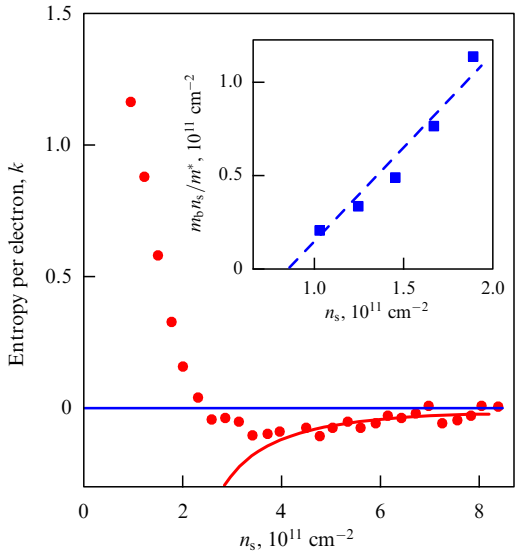

Figure 16. Dependence of $\partial S/\partial n_s$ on the electron concentration (in units of the Boltzmann constant k) at the temperature 3 K (dots). The solid curve was calculated by Eqn (10) with the mass $m_F^* = m_b n_s/(n_s - n_c)$, where $n_c = 8 \times 10^{10}$ cm^{-2}. The inset shows the processing of points in the upper half-plane with Eqn (11). The dashed straight line corresponds to the dependence $m^* = m_b n_s/(n_s - n_c)$ (data from [63]).

The corresponding experimental data are presented in Fig. 16. Here, the solid curve shows calculations with the electron mass at the Fermi level found previously. At an electron density above 4×10^{11} cm^{-2}, the calculation is consistent with experiments. At lower concentrations, experimental points deviate from the calculated curve and even move to the upper half-plane, because the electron system ceases to be degenerate.

In the opposite limit case $kT \geqslant \varepsilon_F$, the authors of [63] processed experimental results using the expression

$$\frac{\partial S}{\partial n_s} = k\left[\frac{\varepsilon_F/kT}{\exp(\varepsilon_F/kT) - 1} - \ln\left(1 - \exp(-\varepsilon_F/kT)\right)\right] \tag{11}$$

for an ideal gas with a renormalized average effective mass m^*.

Expression (11) is valid only in a bounded region of electron concentrations depending on temperature. For example, in Fig. 16 these are concentrations above 10^{11} cm^{-2} (to avoid the insulator) and below 2×10^{11} cm^{-2} (to remain in the nondegenerate regime). The result of the corresponding processing is presented in the inset in Fig. 16. We can see that experimental points in chosen coordinates are close to a straight line with a slope of 45°, extrapolating to a finite electron density.

We note in concluding this section that results obtained in entropy measurements cannot confirm the results in Sections 2.3.3, 2.4.1, and 2.4.2, but do not contradict them either.

2.4.4 Shubnikov–de Haas effect. The parameters of an electron system at the Fermi level can be determined from quantum oscillations of resistance (the Shubnikov–de Haas effect) [65]. Corresponding measurements have been performed by different experimental groups [64, 66–68] with samples from various manufacturers. The effective mass was found from the Lifshitz–Kosevich relations [65],

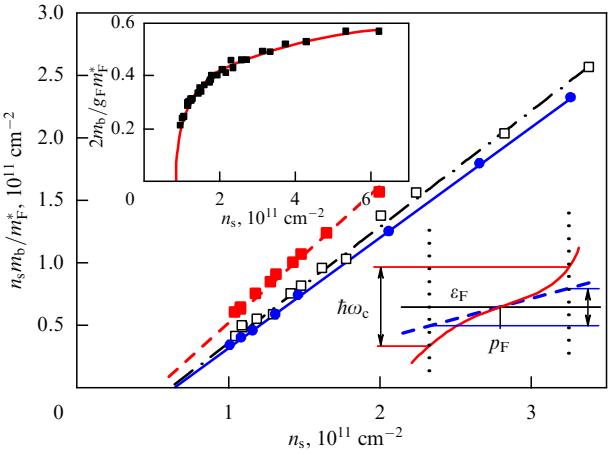

Figure 17. Effective electron mass at the Fermi level extracted from experimental quantum oscillations under the assumption that the Dingle temperature is temperature-independent: unfilled squares [66], dots [67], filled squares (the quantum relaxation time is replaced by the transport time) [66]. Left inset: the product $g_F m_F^*$ measured by quantum oscillation beats [66]. The right inset illustrates the decrease in the measured effective mass caused by the nonlinearity of the electron spectrum near the Fermi level. The dashed line is the result of the semiclassical Bohr–Sommerfeld quantization of electron orbits in the p-space. The right arrow is the expected cyclotron energy in the case of a linear spectrum. The left arrow is the measured cyclotron energy. The flattening of the single-particle spectrum is attached to the Fermi level and shifts together with it with changing the electron concentration or spin polarization. The region of a strong spectral nonlinearity also shifts with it. However, the existence of this effect in silicon MOSFETs has not been conclusively proved in the literature so far.

which give the dependence of the relative magnitude U of quantum oscillations on the temperature and the magnetic field:

$$U = \sum_i U_i^{\mathrm{LK}} \cos\left[\pi \mathrm{i}\left(\frac{\hbar c \pi n_s}{e B_\perp} - 1\right)\right] Z_i^s Z_i^v ,$$
$$U_i^{\mathrm{LK}} = 4 \exp\left(-\frac{2\pi^2 \mathrm{i} k_B T_D}{\hbar\omega_c}\right) \frac{2\pi^2 \mathrm{i} k_B T/\hbar\omega_c}{\sinh(2\pi^2 \mathrm{i} k_B T/\hbar\omega_c)} ,$$
$$Z_i^s = \cos\left(\pi \mathrm{i} \frac{\Delta_Z}{\hbar\omega_c}\right) = \cos\left(\pi \mathrm{i} \frac{g m_F^*}{2 m_e}\right) , \qquad (12)$$
$$Z_i^v = \cos\left(\pi \mathrm{i} \frac{\Delta_v}{\hbar\omega_c}\right) ,$$

where T_D is the Dingle temperature, m_e is the free electron mass, $\hbar\omega_c$ is the cyclotron frequency, Δ_Z is the Zeeman splitting, and Δ_v is the valley splitting.

In weak magnetic fields ($U \ll 1$), the amplitude is determined by the factor U_1^{LK}, and two fitting parameters m_F^* and T_D remain in the temperature dependence in Eqn (12). Such a processing of experimental results from [66] and [67] is shown in Fig. 17.

We can see from Fig. 17 that data obtained for samples from different manufacturers agree with each other within the experimental accuracy, are described well by a linear dependence in corresponding coordinates, and are extrapolated to the concentration of 0.66×10^{11} cm^{-2}.

It was shown in Section 2.4.1 that the transport elastic relaxation time depends on temperature. The questions arise as to whether the temperature dependence can also be manifested in the quantum relaxation time determining the Dingle temperature and if so, how the effective mass changes after processing experimental results with the Dingle temperature depending on temperature. This effect was roughly estimated in [66] by replacing the quantum relaxation time in the Lifshitz–Kosevich formula by the temperature-dependent transport time. The result is shown by filled squares in Fig. 17. Despite quantitative differences with the previous processing, experimental points again lie on a straight line extrapolated to the concentration of 0.55×10^{11} cm^{-2}.

Replacing the quantum relaxation time with the transport time changes the temperature dependence of the Dingle temperature. The critical electron density found from quantum oscillations arguably lies in the interval from 5.5×10^{10} to 6.5×10^{10} cm^{-2}. This value is noticeably lower than that found in Sections 2.4.1 and 2.4.2. The reason for the discrepancy can be the nonlinearity of the single-particle electron spectrum near the Fermi level (see the right inset in Fig. 17). Indeed, at minimal electron densities, the temperature dependence of oscillations is studied at the third or fourth Landau levels, i.e., under the conditions

$$\hbar\omega_c \simeq \frac{1}{3} \frac{p_F v_F}{2} .$$

The nonlinearity of the spectrum for such considerable deviations from the Fermi level can lead to a decrease in the measured effective mass compared with the mass measured directly at the Fermi level.

To avoid misunderstanding, we make an important remark. The amplitude of quantum oscillations is determined exclusively by the vicinity of the Fermi level and is absolutely insensitive to the difference between the band bottom and Fermi energies. For this reason, the measured mass turned out to be insensitive to the spin polarization degree.

The study of the temperature dependence of the amplitude of quantum oscillations in tilted fields [67] revealed another important fact about the independence of the electron mass at the Fermi level from the spin polarization degree. This statement was recently confirmed by independent experiments [64] and by some raw experimental data [66] and calculations [69] for a multi-valley electron system in the weak-coupling limit.

In a tilted magnetic field, another possibility exists for measuring parameters of the electron system at the Fermi level. By changing the tilt angle (or changing one of the components of the magnetic field with the other component kept fixed), the nodes of quantum oscillations can be observed. It was shown in [70] that for a relatively weak electron–electron interaction and zero temperature, the position of the nodes is determined by the product $g_F m_F^*$. The corresponding experimental data presented in the inset in Fig. 17 demonstrate the critical behavior of the product $g_F m_F^*$ but cannot be used to accurately determine the critical concentration because the extrapolation law is unknown.

2.4.5 Low-frequency resistance noise. Information on electron properties at the Fermi level can be obtained by measuring low-frequency resistance noise. Such measurements were performed with Si-MOSFETs of different qualities [71] in a broad temperature range. Below, we consider only the results of low-temperature measurements with the most perfect samples [72, 73].

It was shown that the low-frequency spectral density of noise, which in the metal phase is usually proportional to

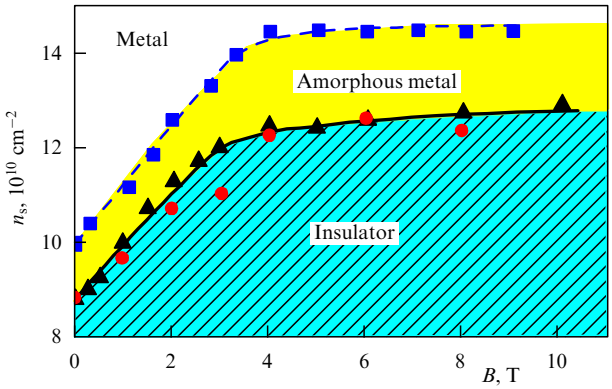

Figure 18. Modified phase diagram for the MIT in a magnetic field parallel to the interface (cf. Fig. 4). The hatched region is the insulator, the filled region is the amorphous metal (data from [73]).

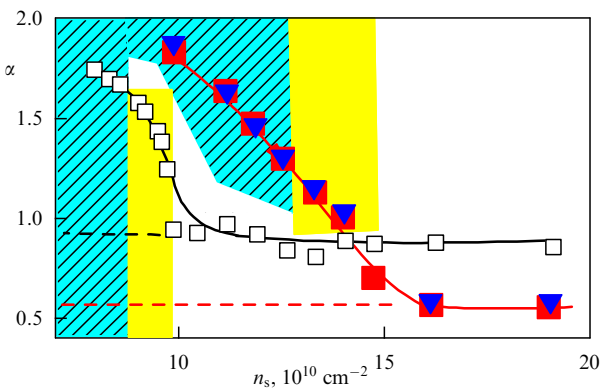

Figure 19. Exponent α of the frequency dependence of the spectral density of low-frequency noise ($\propto 1/f^{\alpha}$) as a function of the electron concentration. Unfilled squares: $B = 0$; triangles and red squares: $B = 4$ T and $B = 9$ T parallel magnetic fields, respectively. The filling corresponds to Fig. 18. The dashed horizontal straight lines show the saturation level of α in the metal phase (data from [73]).

$1/f$, changes in the narrow region above n_c to $1/f^{\alpha}$ with the exponent $\alpha > 1$ increasing with decreasing the electron concentration. The spectral noise density in this region increases for $T < 3$ K with decreasing temperature. Such a behavior is typical for the amorphous phase (glassy phase).

The exponent α in a spin-polarized metal, as in the usual metal phase, is independent of the electron concentration and is $\alpha \simeq 0.5$. In the region of transition from a spin-polarized insulator to a spin-polarized metal [73], α increases, and the concentration range in which a metallic glass phase exists expands (Fig. 18).

While the boundary between an amorphous metal and an insulator can be determined with good accuracy (see Sections 2.1 and 2.2), the upper boundary (dashed curve) in Fig. 18 is somewhat conventional because of the absence of any criterion for the value of the exponent α allowing the separation of the metal phase from the amorphous metal. The accuracy of determining this boundary can be estimated from data presented in Fig. 19.

We note that the electron concentration range where the amorphous metal phase is observed strongly depends on the sample quality [6], considerably expanding with increasing disorder.

2.5 Intermediate conclusions

We briefly formulate the results of the experiments presented above.

(1) The electron mass in the metal phase at the Fermi level increases as the electron density decreases and is independent of the spin polarization degree. The extrapolation predicts a divergence of mass (the appearance of a flat region of the electron spectrum) at the electron concentration close to the MIT point in the zero magnetic field for the best of the samples studied.

(2) In the metal phase, a fraction of localized electrons can be retained, their number being dependent on the sample quality.

(3) In the metal phase, an amorphous metal with long-period correlations of fluctuations can exist in the nearest vicinity of the MIT [72]. In the most perfect samples, the amorphous metal region in the zero magnetic field virtually disappears.

(4) The electron mass averaged over the spectrum in the metal phase also increases with decreasing the electron concentration. More precisely, this statement can be formulated as follows: the distance between the bottom of the electron subband and the Fermi level decreases with decreasing electron density faster than can be expected for a noninteracting electron gas.

(5) The thermodynamic density of states of spin-non-polarized electrons is proportional to the electron mass at the Fermi level. However, this statement should be additionally verified.

(6) The total spin-polarization field is linear in the electron density and is extrapolated for the best samples to zero at the electron concentration close to the concentration of the MIT in the zero magnetic field. This means that the thermodynamic density of states of spin-polarized electrons under the condition $n_s = n_{\uparrow}$ (where $n_{\uparrow}$ is the number of electrons with an energy-advantageous spin orientation) is independent of the electron concentration.

(7) The effective mass of spin-polarized electrons averaged over the spectrum increases as the electron density decreases, demonstrating (by extrapolation) the tendency to diverge at an electron concentration close to that of the MIT in the zero magnetic field.

2.6 Electrons in an insulator

2.6.1 Low-frequency noise in the insulator phase. In [72, 73], measurements of low-frequency noise were extended to the MIT and even into the insulator phase (see Fig. 19). We can see from the figure that neither in the absence of a magnetic field nor in the magnetic field spin-polarizing the electron system were any specific features in the behavior of α observed at the MIT point. Therefore, the transition occurs between the amorphous metal phase (with a finite resistance at the zero temperature) and the glassy insulator phase (with the conductivity tending to zero with decreasing temperature).

The amorphous phase of an insulator was considered in the grating model [74] for spinless electrons. It was shown that in the case of disorder and strong electron–phonon coupling, a gapless state appears with a deep lowering of the single-particle density of states, reaching zero at the Fermi level. With such a spectrum realized, variable-range hopping conductivity should be expected [75]. The temperature dependence of the resistance described by the Efros–Shklovskii law was observed experimentally deep in the insulator [4, 76]. In the region closer to the

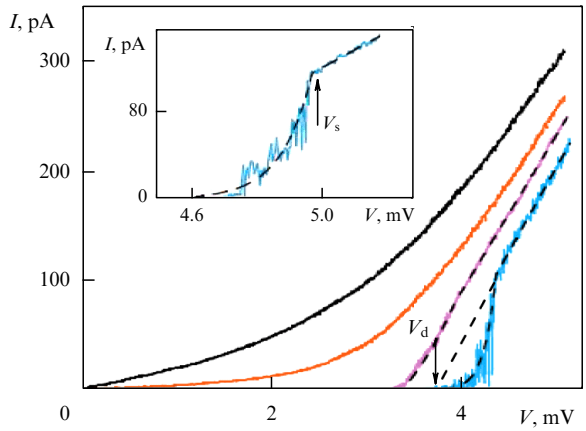

Figure 20. Voltage–current characteristics in the insulator phase. $n_s = 5.36\times 10^{10}$ cm^{-2}, temperature (from right to left): 60, 140, 200, 300 mK. The inset shows the $V-I$ curve at the electron density $n_s = 5.2\times 10^{10}$ cm^{-2} on the expanded scale. $T = 60$ mK. A strong increase in the low-frequency noise is observed in the interval $V_d < V < V_s$ (data from [78]).

MIT, the usual activation dependence was observed [24], demonstrating the transition to nearest-neighbor hopping.

The appearance of an intermediate amorphous metal phase was predicted in [77].

Interesting results on low-frequency noise in the insulator phase were obtained in [78], where nonlinear voltage–current ($V-I$) characteristics were studied in the depth of an insulator (Fig. 20). At a low temperature ($T \simeq 60$ mK) in the linear regime, the current was absent within the experimental accuracy. As the voltage reached a critical value depending on the difference $n_c - n_s$, the current began to increase dramatically, its increase being accompanied by the low-frequency noise, well observed in the inset in Fig. 20. Finally, as the voltage reached the second threshold value, the $V-I$s became linear and the noise amplitude decreased. Both threshold voltages decreased with increasing temperature, the noise decreased, and the current appeared in the linear regime at high temperatures. The slope of the linear part of the $V-I$ curve weakly depended on the temperature (see Fig. 20) and the electron concentration.

The observed $V-I$s are similar (up to the interchange of the current and voltage axes) to the well-known $V-I$s for the depinning of a vortex lattice in type-II superconductors (see, e.g., [79]). Based on this analogy, we can attempt to describe the experimental curves.

Following the terminology used to describe the properties of the vortex lattice, we introduce two critical voltages: the static voltage V_s (see the inset in Fig. 20) corresponding to the onset of the linear dependence of the current on voltage, and the dynamic voltage V_d, the result of extrapolating the linear dependence to zero (see Fig. 20).

The region of voltages $V_d < V < V_s$ is the region of collective pinning of an amorphous electron system with a strong interparticle interaction. In this region, pinning is produced by centers of different strengths, and the electron system can move only due to thermal activation. We note that we are dealing not with the activation of a single electron but with the activation motion of the total electron system or, at least, of a large part of it:

$$I \propto \exp\left[-\frac{U(V)}{kT}\right]. \tag{13}$$

Here, $U(V)$ is the activation energy depending on the potential difference applied to the sample.

For voltages exceeding V_s, the electron system moves with friction, which is maximal at spatial points with the greatest pinning force. Therefore,

$$U_c = eE_sL\,, \tag{14}$$

where U_c is the maximum activation energy in the absence of an electric field, E_s is the electric field at the voltage V_s, and L is the characteristic distance between the points of maximum pinning. It is the random arrangement of these points that supports the amorphous state of the electron system. The electric current in this region linearly depends on the applied voltage,

$$I = \sigma_0(V - V_d)\,, \tag{15}$$

where σ_0 is a coefficient with the dimension of inverse resistance.

Because the activation energy is described by the expression

$$U(V) = U_c - eEL = U_c\left(1 - \frac{V}{V_s}\right), \tag{16}$$

the current at $V < V_s$ is

$$I = \sigma_0(V - V_d)\exp\left[-\frac{U_c(1 - V/V_s)}{kT}\right]. \tag{17}$$

Fitting the experimental curves with expressions (15) and (17) is shown by dashed curves in Fig. 20 and the inset. The only fitting parameter was the activation energy U_c. All other quantities in (15) and (17) were determined from experiments. We can see from Fig. 20 that calculations describe the experiments well.

The noise in the voltage region $V_d < V < V_s$ is related to the expectation of a quite large fluctuation transforming the electron system from one local energy minimum to another. The intense noise in the nonlinear regime and the two-threshold flow disappear earlier than the MIT is reached [78]. Such a behavior agrees well with the noise measurements in the linear regime, where the saturation of α at the level $\alpha \simeq 2$ corresponding to the usual amorphous phase was observed at an electron density noticeably lower than n_c.

2.6.2 Magnetic properties in the insulator phase

Localized droplets. Experimental data presented in [80] were interpreted as the result of the existence of localized droplets in the insulator phase, i.e., localized formations resembling quantum dots consisting of a few ($\simeq 4$) electrons. Electrons in such droplets are completely spin-polarized with a random orientation of the total magnetic moment in the zero magnetic field.

Despite identical names, it is unlikely that localized droplets have something in common with the free droplets proposed in [81] as one of the intermediate phases between a metal and a Wigner crystal.

In the framework of the concept of localized droplets, the magnetic moment of a unit area can be written as

$$M = \mu_B\left[n_d \tanh(sb) + (n_s - n_d)\tanh(b)\right], \tag{18}$$

where n_d is the electron density in droplets, s is the mean number of electrons in one droplet, and $b = \mu_B B/kT$ is the

normalized magnetic field. For simplicity, we assume that $s \gg 1$ and $b \ll 1$. Then

$$\frac{\partial M}{\partial n_s} \simeq N_d \frac{\partial s}{\partial n_s} \left[\tanh(sb) + sb\cosh^{-2}(sb)\right], \quad (19)$$

where $N_d = n_d/s$ is the number of droplets (strong pinning centers), weakly depending on the electron concentration in the insulator phase but depending on temperature.

Figure 21 shows fitting curves based on expression (19) for the values of the fitting parameter $N_d \partial s/\partial n_s$ equal to 2, 1, -0.1, and $s = 4$. We can see that the fitting curves describe the experiments well.

A comparison of calculations with experiments leads to some interesting conclusions. First, the value of the derivative $\partial M/\partial n_s \simeq 2$ at the temperature $T = 0.8$ K means that at lower concentrations this derivative is considerably smaller than unity and the interval of its large values is quite narrow. This statement is inconsistent with higher-temperature measurements (see, e.g., Fig. 12). Second, the number of localized droplets turns out to be temperature-dependent (which requires additional verification, however) and weakly dependent on the electron concentration in the insulator phase. Third, after transition to the metal phase, the derivative $\partial s/\partial n_s$ changes its sign.

A question naturally arises: How are the concepts of localized droplets and the amorphous phase following from noise measurements described above related? Taking into account that the Coulomb energy considerably exceeds the temperature for $T \leqslant 2$ K, we see that the characteristic spatial scale between electrons in a droplet should not differ significantly from the mean distance between electrons. In other words, the density of an electron system with droplets weakly changes at scales exceeding (slightly) the mean distance between electrons, which corresponds to the amorphous state and is qualitatively confirmed by experiments, albeit those performed with samples of different qualities prepared by different manufacturers.

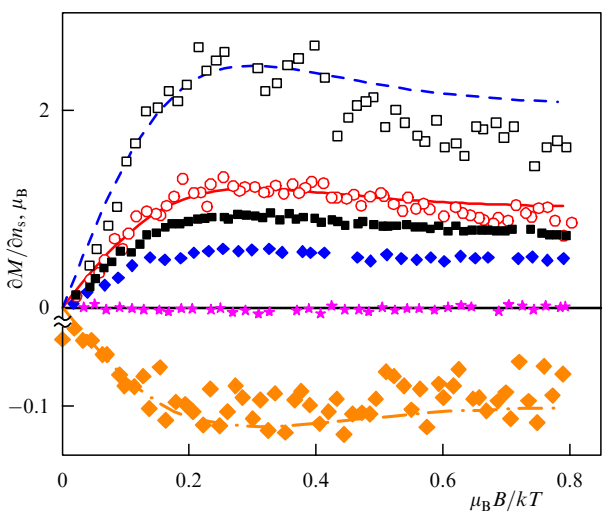

Figure 21. Derivative of the magnetic moment of a unit area by the electron concentration as a function of the normalized magnetic field parallel to the MOSFET interface. Unfilled symbols: $n_s = 5 \times 10^{10}$ cm^{-2}, squares ($T = 0.8$ K), circles ($T = 1.2$ K). Filled symbols: $T = 1.8$ K: squares, diamonds, stars, and large diamonds correspond to respective electron concentrations 0.4, 0.8, 1.4, 2.5 ($\times 10^{11}$) cm^{-2}. The dashed, solid, and dashed-dotted curves are fittings using Eqn (19) (data from [80]).

Magnetic moment and susceptibility in the insulator phase. We again consider Fig. 12. In a magnetic field of 2 T, the magnetic moment increases linearly with a unit slope up to a concentration of 5×10^{10} cm^{-2}. As the electron concentration is increased further, the magnetic moment continues to increase, but now proportionally to n_s. Because $B = 2$ T at the temperature 1.7 K corresponds to the saturation of the magnetic moment of droplets, we have to conclude that for $n_s > 5 \times 10^{10}$ cm^{-2}, not all localized electrons enter droplets. Therefore, the number of strong pinning centers is $n_d \sim 5 \times 10^{10}/s \sim 1.2 \times 10^{10}$ cm^{-2} ($s = 4$), and in the metal phase, according to the estimate in Section 2.3.3, $s \sim 2$.

In the magnetic field $B = 5$ T at the temperature $T = 0.4$ K, the parameter $b \simeq 16$ and all electrons in the insulator phase are spin-polarized. It can be expected that the straight line $M = \mu_B n_s$ specifies the behavior of the magnetic moment in the insulator phase, in agreement with the results in [52, 54]. However, as follows from Fig. 11, experimental points in the metal phase at the minimal concentration are higher than this straight line, which is unsurprising because the Lande factor is $g > 2$ in the metal phase.

The susceptibility in the insulator phase is determined by the initial region of the curve describing the dependence of the magnetic moment on the magnetic field. In the concept of droplets,

$$\chi = \frac{\mu_B^2}{kT}\left[n_d(s-1) + n_s\right]. \quad (20)$$

In [80], the relation $n_d \propto 1/T$ was observed to roughly hold.

In the initial part of the dependence $\chi(n_s)$, the susceptibility is proportional to concentration (see Fig. 13); therefore, $n_d = n_s$. The slope of the initial part of the sample shown by squares in Fig. 13 is 30% smaller than that for a sample whose data are shown by circles. According to (20), this means that the mean number s of particles in a droplet is smaller for a more perfect sample than for a more disordered sample.

2.7 Additional intermediate conclusions

We note that neither of the two alternative naive models presented in Section 2.3.1 is fully correct. Only their combination is consistent with experiments.

Indeed, in the metal phase, both the energy-averaged effective electron mass (m^*) and the effective electron mass (m_F^*) at the Fermi level increase with decreasing the electron concentration. We note that m_F^* exhibits a tendency to diverge, in agreement with the second model, assuming that localized electrons are absent in the metal phase and the properties of the electron system are determined only by interaction. At the same time, the metal phase undoubtedly contains a small number of localized electrons, which, for example, determine the magnetic susceptibility of the electron system. The number of localized electrons depends on the sample quality. Experiments demonstrate that according to the assumptions of the first model, the presence of localized electrons in the metal phase does not affect the Hall effect in weak fields.

The insulator phase in the general case contains electrons included in localized droplets, with the total magnetic moment of the droplet behaving as a single whole, and also localized electrons not entering the droplets. The relation between these two electron groups probably depends on the sample quality. Some properties of this mixture, for example,

noise characteristics, are similar to those of the amorphous phase. Unfortunately, any theoretical calculations concerning the magnetic properties of a strongly coupled disordered electron system are absent.

Studying the magnetic moment at the MIT at millikelvin temperatures could be of great interest. The extrapolation of the available information predicts a jump in the magnetic moment in this region.

3. Electrons in SiGe/Si/SiGe quantum wells

3.1 Advantages and disadvantages of the structures

The properties of electrons in the highest-mobility SiGe/Si/SiGe quantum wells were studied in [82–87]. We consider the results of studies [85–87] in which electrons were located in a (100) silicon quantum well 150 Å in width. The quantum well was bounded from above and at the bottom by SiGe barriers. The top barrier $\sim$ 1500 Å in width was covered with a 10 Å thick silicon layer with thermally deposited 2000 – 3000 Å thick SiO and a metal gate. The samples, as in the Si-MOSFET case, had the shape of Hall bridges.

The advantages of the electron system in quantum wells in SiGe/Si/SiGe systems are due to, first, the high electron mobility and, second, the feasibility of measurements at low electron concentrations. The dependence of electron mobility on the electron concentration for one of the best samples is shown in Fig. 22. We can see that the maximum electron mobility in an SiGe/Si/SiGe quantum well is almost two orders of magnitude greater than the electron mobility in the best Si-MOSFETs. In addition, metal conductivity is observed down to very low electron concentrations of the order of 1.5×10^{10} cm^{-2}.

Among the disadvantages is a weaker (at a fixed concentration) electron–electron interaction. As already mentioned in the Introduction, the reason is the dielectric constant greater by a factor of 1.5 and a greater spread of the electron wave function in the direction normal to the interface.

Another disadvantage of SiGe/Si/SiGe structures is a complex surface relief (see the inset in Fig. 22). The relief has 'ridges' extended along the [110] and [−110] directions with a characteristic height of $\sim$ 50 nm and period of 10 μm. The relief is rather flat, because the period greatly exceeds the characteristic ridge height. It was shown in [80] that the potential well relief repeats the surface relief, and therefore the modulation of the electron concentration caused by ridges is virtually absent.

Nevertheless, the relief modulation considerably complicates measurements in a magnetic field parallel to the surface. Although the field is parallel to the surface on average, the bends of the quantum well lead to the appearance of a local normal (in the ideal case, alternating) component. We can no longer assume that the parallel field acts only on the electron spin, because the local normal component acts on the orbital motion. This difficulty can be eliminated by a proper choice of the orientation of the Hall bridge with respect to crystallographic axes and the magnetic field orientation with respect to the measuring current [86, 87].

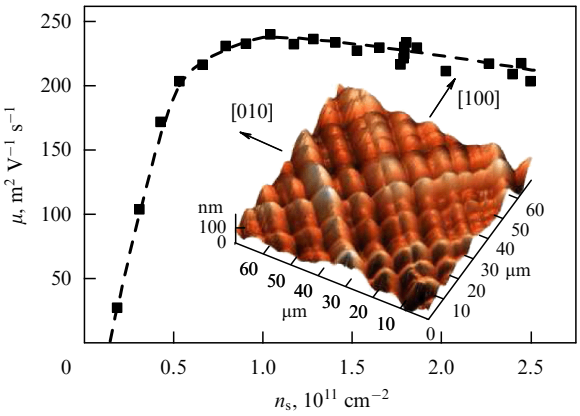

Figure 22. Electron mobility in a (100) Si/SiGe quantum well as a function of the electron concentration at $T = 50$ mK. The inset shows an atomic-force microscope scan of the sample surface (before the deposition of an SiO insulator and a metal gate) [85, 86].

3.2 Tendency of a flat band to appear at the Fermi level

The electron system in SiGe/Si/SiGe quantum wells was used for measurements of two types [87]. First, the total spin-polarization field was measured as a function of the electron density. The corresponding results are shown in Fig. 23.

The observed behavior of the total spin-polarization field is highly consistent (albeit up to a numerical coefficient) with Monte Carlo simulations [49]. At high concentrations, the dependence is well approximated by a straight line tending to a finite concentration as $B^{\mathrm{p}} \to 0$. At a concentration approximately equal to $n_s \simeq 7 \times 10^{10}$ cm^{-2}, the dependence exhibits a break and $B^{\mathrm{p}}(n_s)$ tends to the origin at lower concentrations (the dashed line in the left inset in Fig. 23).

The right inset in Fig. 23 shows the dependence of $m_b n_s / m_F^*$ on n_s. We discuss the method for experimentally measuring the electron mass at the Fermi level below, and now note the linear dependence in the right inset extrapolating to a finite electron concentration, which coincides within

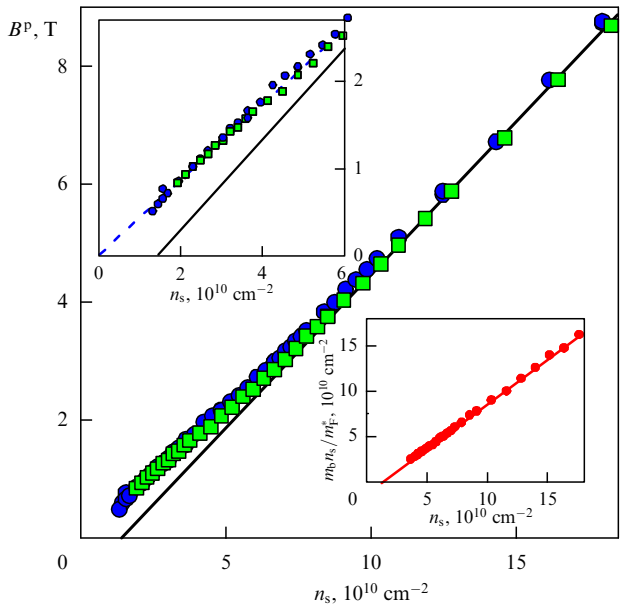

Figure 23. Total spin-polarization fields for two samples (different symbols) at temperature 30 mK as a function of the electron density. The straight line is a linear fitting to points at large concentrations. The left inset is the initial part of the same dependence on an expanded scale. The right inset is the concentration dependence of the inverse effective mass at the Fermi level [87].

the experimental accuracy with the result of the extrapolation of the dependence $B^{\mathrm{p}}(n_{\mathrm{s}})$. As mentioned above, this dependence is determined by the energy-averaged mass. Therefore, at high concentrations, the energy-averaged electron mass and the electron mass at the Fermi level are at least proportional to each other, if not coincident. At the same time, at concentrations $n_{\mathrm{s}} < 7 \times 10^{10}$ cm^{-2}, the behavior of the masses is completely different: the electron mass at the Fermi level continues to increase with decreasing the electron concentration, whereas the energy-averaged mass saturates.

Such a behavior is more clearly demonstrated in Fig. 24, where the dependences of $g_{\mathrm{F}}m^*$ and $g_{\mathrm{F}}m_{\mathrm{F}}^*$ on the electron concentration are compared. The first dependence was found by using experimental points $B^{\mathrm{p}}(n_{\mathrm{s}})$ and the relation

$$g_{\mathrm{F}}\mu_{\mathrm{B}}B^{\mathrm{p}} = \frac{2\pi\hbar^2 n_{\mathrm{s}}}{m^* g_{\mathrm{v}}}\,, \tag{21}$$

where $g_{\mathrm{v}} = 2$ is the valley degeneracy. The dependence $g_{\mathrm{F}}m_{\mathrm{F}}^*(n_{\mathrm{s}})$ was obtained from Eqns (12). The dependence of the resistance on the magnetic field was fitted as shown in the inset in Fig. 24. The fitting parameters were m_{F}^*, $T_{\mathrm{D}}m_{\mathrm{F}}^*$, and $g_{\mathrm{F}}m_{\mathrm{F}}^*$. The value of m_{F}^* was found in separate experiments from the temperature dependence of quantum oscillations with an accuracy of 10%. The fitting of experimental curves turned out to be not very sensitive to the parameters m_{F}^* and $T_{\mathrm{D}}m_{\mathrm{F}}^*$ but was rather sensitive to the product $g_{\mathrm{F}}m_{\mathrm{F}}^*$.

A comparison of the behavior of $g_{\mathrm{F}}m_{\mathrm{F}}^*$ and $g_{\mathrm{F}}m^*$ at concentrations $n_{\mathrm{s}} < 7 \times 10^{10}$ cm^{-2} clearly demonstrates the difference: the electron mass at the Fermi level continues to increase with decreasing concentration, whereas the energy-averaged mass saturates. Such a behavior corresponds to the appearance of a flat part of the single-particle spectrum at the Fermi level (Fig. 25).

In the vicinity of the critical concentration $\simeq 1.4 \times 10^{10}$ cm^{-2}, the electron system is in the critical region where the effective mass at the Fermi level is limited by the temperature $m_{\mathrm{F}}^* < p_{\mathrm{F}}\Delta p/4kT$. The data presented in Fig. 24 give the estimate of the interval Δp: $\Delta p/p_{\mathrm{F}} = 0.06$.

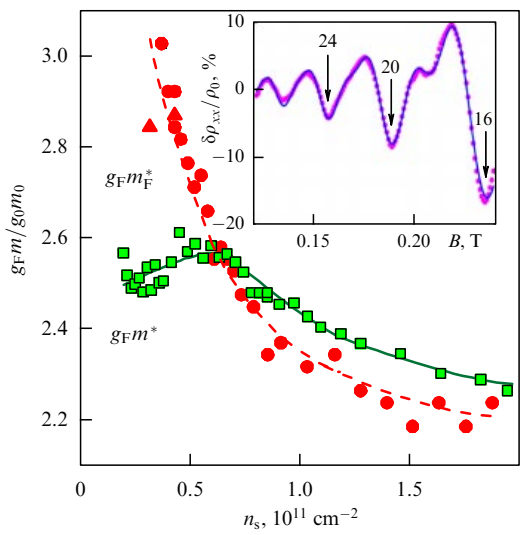

Figure 24. Comparison of the concentration dependences of the energy-averaged electron mass and the mass at the Fermi level. $T = 30$ mK. The lines are guides for the eye. The inset illustrates the quality of fitting the experimental dependence of the normalized resistance using expression (12) [87].

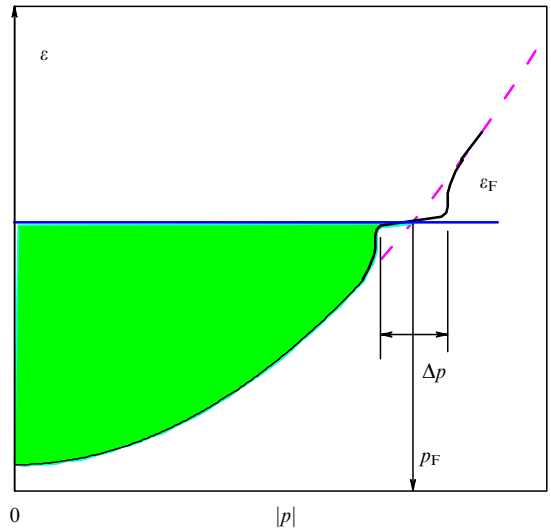

Figure 25. Assumed single-particle spectrum with a flat region at the Fermi level. The energy and momentum region occupied by electrons is shown by filling.

We note that the appearance of the interaction-induced flat part of the single-particle spectrum at the Fermi level was predicted in theoretical papers (see, e.g., [88, 89]) based on absolutely different ideas.

Both experiments presented above and the conclusion on the different behaviors of the electron mass at the Fermi level and the energy-averaged mass are quite unusual. To confirm this behavior, independent experiments are required. Such an experiment was discussed in [92].

4. Conclusions

By comparing the results obtained by different research groups for different Si-MOSFET samples with the results of measurements with SiGe/Si/SiGe quantum wells, we can conclude that the effective electron mass m_{F}^* at the Fermi level in the metal phase tends to diverge as the electron concentration decreases. The results of measurements of the effective mass at the Fermi level performed by various groups with samples of the same type from different manufacturers differ only due to different processing methods. Unfortunately, the increase in m_{F}^* in the region available for measurements is not as considerable as, for example, in ^{3}He films [90, 91], and the conclusion about the divergence of the mass has to be made based on extrapolation.

In the metal phase, a small amount (depending on the sample) of localized electrons weakly affecting transport properties is observed.

In the insulator phase and in the MIT vicinity, the electron system reveals properties typical of amorphous media with strongly interacting particles. The study of the microscopic structure of the insulator phase in Si-MOSFET has shown that it consists of localized droplets (resembling quantum dots) containing on average about four spin-polarized electrons, and of localized electrons outside such droplets.

A simple listing demonstrates the considerable recent progress in experiments that has been achieved due to the development of experimental methods. Unfortunately, the quality of Si-MOSFETs has not improved. On the other hand, the study of electrons in SiGe/Si/SiGe quantum wells is

far from comprehensive, and conclusions made based on the available experimental data are only preliminary. Independent additional experiments are described in [92]. Nevertheless, to reliably prove the possible independence of the MIT from events at the Fermi level, further experiments are required.

Acknowledgements
The author thanks A A Shashkin and S V Kravchenko for the useful discussions. The author especially thanks V M Pudalov for reading the manuscript and the numerous remarks. The study was partially supported by the Russian Foundation for Basic Research (grant no. 18-02-00368) and the State Program of the Institute of Solid State Physics, RAS.

References

1. Abrahams E et al. *Phys. Rev. Lett.* **42** 673 (1979)
2. Kravchenko S V et al. *Phys. Rev. B* **50** 8039 (1994)
3. Zavaritskaya T N, Zavaritskaya E I *JETP Lett.* **45** 609 (1987); *Pis'ma Zh. Eksp. Teor. Fiz.* **45** 476 (1987)
4. Kravchenko S V et al. *Phys. Rev. B* **51** 7038 (1995)
5. Kravchenko S V, Klapwijk T M *Phys. Rev. Lett.* **84** 2909 (2000)
6. Popović D, in *Strongly Correlated Electrons in Two Dimensions* (Ed. S V Kravchenko) (Singapore: Pan Stanford Publ., 2017)
7. Feng X G et al. *Phys. Rev. Lett.* **86** 2625 (2001)
8. Finkel'stein A M *Sov. Phys. JETP* **57** 97 (1983); *Zh. Eksp. Teor. Fiz.* **84** 168 (1983)
9. Finkel'stein A M *Sov. Sci. Rev. A* **14** 3 (1990)
10. Punnoose A, Finkel'stein A M *Science* **310** 289 (2005)
11. Punnoose A, Finkel'stein A M *Phys. Rev. Lett.* **88** 016802 (2001)
12. Anissimova S et al. *Nature Phys.* **3** 707 (2007)
13. Knyazev D A et al. *Phys. Rev. Lett.* **100** 046405 (2008)
14. Punnoose A et al. *Phys. Rev. B* **82** 201308(R) (2010)
15. Gold A, Dolgopolov V T *Phys. Rev. B* **33** 1076 (1986)
16. Zala G, Narozhny B N, Aleiner I L *Phys. Rev. B* **64** 214204 (2001)
17. Abrahams E, Kravchenko S V, Sarachik M P *Rev. Mod. Phys.* **73** 251 (2001)
18. Kravchenko S V, Sarachik M P *Rep. Prog. Phys.* **67** 1 (2004)
19. Pudalov V M, in *The Electron Liquid Paradigm in Condensed Matter Physics* (Eds G F Giuliani, G Vignale) (Amsterdam: IOS Press, 2004)
20. Shashkin A A *Phys. Usp.* **48** 129 (2005); *Usp. Fiz. Nauk* **175** 139 (2005)
21. Kravchenko S V, Sarachik M P *Int. J. Mod. Phys. B* **24** 1640 (2010)
22. Shashkin A A, Kravchenko S V, in *Strongly Correlated Electrons in Two Dimensions* (Ed. S V Kravchenko) (Singapore: Pan Stanford Publ., 2017)
23. Gantmakher V F, Dolgopolov V T *Phys. Usp.* **51** 3 (2008); *Usp. Fiz. Nauk* **178** 3 (2008)
24. Shashkin A A, Kravchenko S V, Klapwijk T M *Phys. Rev. Lett.* **87** 266402 (2001)
25. Sarachik M P, Kravchenko S V *Proc. Natl. Acad. Sci. USA* **96** 5900 (1999)
26. Pudalov V M et al. *Phys. Rev. B* **60** R2154 (1999)
27. Vitkalov S A et al. *Phys. Rev. Lett.* **85** 2164 (2000)
28. Pudalov V M et al. *Phys. Rev. Lett.* **88** 076401 (2002)
29. Shashkin A A, Kravchenko S V, Dolgopolov V T *JETP Lett.* **58** 220 (1993); *Pis'ma Zh. Eksp. Teor. Fiz.* **58** 215 (1993)
30. Kravchenko S V et al. *Phys. Rev. Lett.* **75** 910 (1995)
31. Eng K et al. *Phys. Rev. Lett.* **88** 136402 (2002)
32. Dolgopolov V T, Shashkin A A, Kravchenko S V *Phys. Rev. B* **96** 075307 (2017)
33. Jaroszyński J, Popović D, Klapwijk T M *Phys. Rev. Lett.* **92** 226403 (2004)
34. Lozovik Yu E, Yudson V I *JETP Lett.* **22** 11 (1975); *Pis'ma Zh. Eksp. Teor. Fiz.* **22** 26 (1975)
35. Khmelnitskii D E *Phys. Lett. A* **106** 182 (1984)
36. Dolgopolov V T *Phys. Usp.* **57** 105 (2014); *Usp. Fiz. Nauk* **184** 113 (2014)
37. Pudalov V M, in *Physics of the Electron Solid* (Conf. Proc. and Lecture Notes in Applied Physics, Vol. 1, Ed. S T Chui) (Cambridge, MA: International Press, 1994)
38. Dolgopolov V T *Phys. Usp.* **60** 731 (2017); *Usp. Fiz. Nauk* **187** 785 (2017)
39. Shashkin A A et al. *Phys. Rev. Lett.* **87** 086801 (2001)
40. Vitkalov S A et al. *Phys. Rev. Lett.* **87** 086401 (2001)
41. Pudalov V M et al., cond-mat/0103087
42. Shashkin A A et al. *Phys. Rev. Lett.* **96** 036403 (2006)
43. Dolgopolov V T, Gold A *Phys. Rev. Lett.* **89** 129701 (2002)
44. Gold A, Dolgopolov V T *J. Phys. Condens. Matter* **14** 7091 (2002)
45. Pudalov V M et al. *Phys. Rev. Lett.* **88** 196404 (2002)
46. Pudalov V M et al. *JETP Lett.* **80** 359 (2004); *Pis'ma Zh. Eksp. Teor. Fiz.* **80** 408 (2004)
47. Shashkin A A et al. *Phys. Rev. B* **66** 073303 (2002)
48. Anissimova S et al. *Phys. Rev. Lett.* **96** 046409 (2006)
49. Fleury G, Waintal X *Phys. Rev. B* **81** 165117 (2010)
50. Dolgopolov V T *JETP Lett.* **101** 282 (2015); *Pis'ma Zh. Eksp. Teor. Fiz.* **101** 300 (2015)
51. Gold A, Dolgopolov V T *JETP Lett.* **86** 600 (2007); *Pis'ma Zh. Eksp. Teor. Fiz.* **86** 687 (2007)
52. Prus O et al. *Phys. Rev. B* **67** 205407 (2003)
53. Reznikov M, Sivan U, cond-mat/0410409
54. Teneh N et al., arXiv:0910.5724
55. Reznikov M et al. *JETP Lett.* **92** 470 (2010); *Pis'ma Zh. Eksp. Teor. Fiz.* **92** 518 (2010)
56. Stern F *Phys. Rev. Lett.* **44** 1469 (1980)
57. Dorozhkin S I, Dolgopolov V T *JETP Lett.* **40** 1019 (1984); *Pis'ma Zh. Eksp. Teor. Fiz.* **40** 245 (1984)
58. Mokashi A et al. *Phys. Rev. Lett.* **109** 096405 (2012)
59. Fletcher R et al. *Phys. Rev. B* **56** 12422 (1997)
60. Faniel S et al. *Phys. Rev. B* **76** 161307(R) (2007)
61. Goswami S et al. *Phys. Rev. Lett.* **103** 026602 (2009)
62. Dolgopolov V T, Gold A *JETP Lett.* **94** 446 (2011); *Pis'ma Zh. Eksp. Teor. Fiz.* **94** 481 (2011)
63. Kuntsevich A Y et al. *Nature Commun.* **6** 7298 (2015)
64. Pudalov V M, Gershenson M E, Kojima H *Phys. Rev. B* **90** 075147 (2014)
65. Lifshitz I M, Kosevich A M *Sov. Phys. JETP* **2** 730 (1956); *Zh. Eksp. Teor. Fiz.* **29** 636 (1955)
66. Pudalov V M et al. *Phys. Rev. Lett.* **88** 196404 (2002)
67. Shashkin A A et al. *Phys. Rev. Lett.* **91** 046403 (2003)
68. Klimov N N et al. *Phys. Rev. B* **78** 195308 (2008)
69. Gangadharaiah S, Maslov D L *Phys. Rev. Lett.* **95** 186801 (2005)
70. Bychkov Yu A, Gor'kov L P *Sov. Phys. JETP* **14** 1132 (1962); *Zh. Eksp. Teor. Fiz.* **41** 1132 (1962)
71. Popovic D, in *Conductor Insulator Quantum Transitions* (Eds V Dobrosavljević, N Trivedi, J M Valles (Jr.)) (Oxford: Oxford Univ. Press, 2012)
72. Jaroszyński J, Popović D, Klapwijk T M *Phys. Rev. Lett.* **89** 276401 (2002)
73. Jaroszyński J, Popović D, Klapwijk T M *Phys. Rev. Lett.* **92** 226403 (2004)
74. Pastor A A, Dobrosavljević V *Phys. Rev. Lett.* **83** 4642 (1999)
75. Efros A L, Shklovskii B I *J. Phys. C* **8** L49 (1975)
76. Pudalov V M et al. *Phys. Rev. Lett.* **70** 1866 (1993)
77. Dobrosavljević V, Tanasković D, Pastor A A *Phys. Rev. Lett.* **90** 016402 (2003)
78. Brussarski P et al. *Nature Commun.* **9** 3803 (2018)
79. Blatter G et al. *Rev. Mod. Phys.* **66** 1125 (1994)
80. Teneh N et al. *Phys. Rev. Lett.* **109** 226403 (2012)
81. Spivak B, Kivelson S A *Phys. Rev. B* **70** 155114 (2004)
82. Kawai M et al. *Appl. Phys. Lett.* **94** 82102 (2009)
83. Lu T M et al. *Appl. Phys. Lett.* **97** 059904 (2010)
84. Huang S-H et al. *Appl. Phys. Lett.* **101** 042111 (2012)
85. Melnikov M Yu et al. *Appl. Phys. Lett.* **106** 092102 (2015)
86. Melnikov M Yu et al. *J. Appl. Phys.* **122** 224301 (2017)
87. Melnikov M Yu et al. *Sci. Rep.* **7** 14539 (2017)
88. Khodel V A, Shaginyan V R *JETP Lett.* **51** 553 (1990); *Pis'ma Zh. Eksp. Teor. Fiz.* **51** 488 (1990)
89. Camjayi A et al. *Nature Phys.* **4** 932 (2008)
90. Casey A et al. *J. Low Temp. Phys.* **113** 293 (1998)
91. Casey A et al. *Phys. Rev. Lett.* **90** 115301 (2003)
92. Melnikov M Yu et al. *Phys. Rev. B* **99** 081106(R) (2019)